



Article

Sea Ice Extent Retrieval Using CSCAT 12.5 km Sampling Data

Liling Liu ^{1,2,*} , Xiaolong Dong ³ , Liqing Yang ⁴, Wenming Lin ⁴ and Shuyan Lang ⁵¹ School of Artificial Intelligence, China University of Mining and Technology, Beijing 100083, China² Key Laboratory of Space Ocean Remote Sensing and Application, Ministry of Natural Resources, Beijing 100081, China³ The CAS Key Laboratory of Microwave Remote Sensing, National Space Science Center, Chinese Academy of Sciences, Beijing 100190, China; dongxiaolong@mirslab.cn⁴ School of Marine Sciences, Nanjing University of Information Science & Technology, Nanjing 210044, China; 20191237011@nuist.edu.cn (L.Y.); wenminglin@nuist.edu.cn (W.L.)⁵ National Satellite Ocean Application Service, Beijing 100081, China; langshuyan@mail.nsoas.org.cn

* Correspondence: liuliling@cumtb.edu.cn

Abstract: Polar sea ice extent exhibits a highly dynamic nature. This paper investigates the sea ice extent retrieval on a fine (6.25 km) grid based on the 12.5 km sampling data from the China France Ocean Satellite Scatterometer (CSCAT), which is generated by an adapted Bayesian sea ice detection algorithm. The CSCAT 12.5 km sampling data are analyzed, a corresponding sea ice GMF model is established, and the important calculation procedures and parameter settings of the adapted Bayesian algorithm for CSCAT 12.5 km sampling data are elaborated on. The evolution of the sea ice edge and extent based on CSCAT 12.5 km sampling data from 2020 to 2022 is introduced and quantitatively compared with sea ice extent products of Advanced Microwave Scanning Radiometer 2 (AMSR2) and the Advanced Scatterometer onboard MetOp-C (ASCAT-C). The results suggest the sea ice extent of CSCAT 12.5 km sampling data has good consistency with AMSR2 at 15% sea ice concentration. The sea ice edge accuracy between them is about 7 km and 10 km for the Arctic and Antarctic regions, and their sea ice extent difference is 0.25 million km² in 2020 and 0.5 million km² in 2021 and 2022. Compared to ASCAT-C 12.5 km sampling data, the sea ice edge Euclidean distance (ED) of CSCAT 12.5 km data is 14 km (2020 and 2021) and 12.5 km (2022) for the Arctic region and 14 km for the Antarctic region. The sea ice extent difference between them is small except for January to May 2020 and 2021 for the Arctic region. There are significant deviations in the sea ice extents of CSCAT 12.5 km and 25 km sampling data, and their sea ice extent difference is 0.3–1.0 million km².

Keywords: scatterometer; CSCAT; sea ice extent; sea ice edge

Citation: Liu, L.; Dong, X.; Yang, L.; Lin, W.; Lang, S. Sea Ice Extent Retrieval Using CSCAT 12.5 km Sampling Data. *Remote Sens.* **2024**, *16*, 700. <https://doi.org/10.3390/rs16040700>

Academic Editor: Yi Luo

Received: 8 January 2024

Revised: 10 February 2024

Accepted: 13 February 2024

Published: 16 February 2024



Copyright: © 2024 by the authors. Licensee MDPI, Basel, Switzerland. This article is an open access article distributed under the terms and conditions of the Creative Commons Attribution (CC BY) license (<https://creativecommons.org/licenses/by/4.0/>).

1. Introduction

The observation and characterization of the polar cryosphere are crucial for understanding the changes in the Earth's climate system. The polar cryosphere is composed mainly of surfaces covered by glaciers, sea ice, and open ocean. The properties of sea ice (i.e., extent, variability, physical characteristics) have profound impacts on the climate and can respond quickly to changes in atmospheric and oceanic forces. Because of the large spatial coverage, spaceborne sensors are an effective means of monitoring polar sea ice. At present, polar sea ice is observed through a series of active and passive microwave sensors, as well as a wide range of electromagnetic spectra [1]. The passive microwave sensors (or radiometers) have provided global sea ice monitoring data over four decades. In recent years, the global observations of sea ice mainly relied on Advanced Microwave Scanning Radiometer for EOS (AMSR-E) from 2002 to 2011 and Advanced Microwave Scanning Radiometer 2 (AMSR2) since 2012. These two sensors offer much higher resolution data than other radiometers due to their larger antenna reflector diameters. For AMSR2, the average resolution for each frequency channel is 49 km (6.93/7.3 GHz), 33 km (10.65 GHz),

18 km (18.7 GHz), 15 km (23 GHz), 10 km (36.5 GHz), and 4 km (89.0 GHz) [2]. As the frequency increases, the resolution also improves. The sea ice extent product is usually generated from sea ice concentration data from microwave radiometers. The grid resolution of the available sea ice concentration data is 25 km, 12.5 km, 10 km, 6.25 km, and 3.125 km [3–5]. A high grid resolution is achieved by increasing the operating frequency of the radiometers. However, high frequencies increase the sensitivity of brightness temperature to atmospheric factors such as clouds, liquid water, and comprehensive water vapor, which in turn affects the accuracy of sea ice extent retrieval [6]. Therefore, researchers proposed the active and passive multiple polarization sea ice detection scheme to improve the accuracy of sea ice extent retrieval [7]. The active microwave sensors include Synthetic Aperture Radars (SARs), altimeters, and scatterometers, where SARs and altimeters are not suitable for large-scale polar sea ice extent retrieval. For scatterometers, the retrieved sea ice extents are on the grids of 25 km and 12.5 km [8–12]. Therefore, this paper investigates the application of the existing scatterometer data to generate sea ice extent mapping with higher grid resolution (i.e., 6.25 km).

Since the 1990s, a series of C-band and Ku-band scatterometers have been launched. Table 1 shows the spaceborne scatterometers launched from 2016 to the present. These scatterometers can be divided into two types by the antenna beam: pencil beam scatterometers (such as Oceansat Scatterometer, OSCAT; and HY-2 Scatterometer, HSCAT) and fan beam scatterometers (such as Advanced Scatterometer, ASCAT; China French Ocean Satellite Scatterometer, CSCAT; and Wind Radar, WindRad). The pencil beam scatterometers typically operate in the Ku band, providing diversity in azimuth measurements through antenna rotation, but with limited incident angles. The fan beam scatterometers allow for measurements of multiple incident angles (28–53° in mid beams and 37–64° in front/after beams for ASCAT; 28–51° for CSCAT; 36–45° in the C band and 37–43° in the Ku band for WindRad) and multiple azimuth angles (six fixed antennas in different directions for ASCAT, rotating antennas for CSCAT and WindRad) [10,13,14]. Compared with the pencil beam scatterometers, the sampling data of the fan beam scatterometers, such as ASCAT, CSCAT, and WindRad (Ku band), have higher-resolution sampling data, with a maximum value of 12.5 km [15,16]. That is because the spatial resolution of these fan-shaped beams is about 10 km. It is worth noting that this spatial resolution is equivalent to that of AMSR2 at 36.5 GHz, but the corresponding operating frequency of the scatterometers is much lower. The high-resolution (12.5 km) sampling data of the fan beam scatterometers (ASCAT, CSCAT, and WindRad in the Ku band) provide the possibility to retrieve large-scale sea ice extents on a 6.25 km grid.

Table 1. The spaceborne scatterometers launched since 2016.

Year	Satellite	Sensor	Frequency	Views	Sampling	Swath
2016–2018–2020–2021–	ScatSat-1 HY-2B HY-2C HY-2D	OSCAT HSCAT	13.5 GHz, Ku band 13.25 GHz, Ku band	2–4 2–4	50/25 km 50/25 km	1400/1800 km 1350/1700 km
2018–2019–2023	MetOp-C CFOSAT	ASCAT CSCAT	5.255 GHz, C band 13.26 GHz, Ku band	3 2–16	25/12.5 km 25/12.5 km	2 × 550 km >1000 km
2021–	FY-3E	WindRad	5.4 GHz, C band 13.256 GHz, Ku band	2–16	25/12.5 km	>1200 km

Different from ASCAT, CSCAT and WindRad adopt a novel rotating fan beam observation geometry and operate in dual polarization (vertical-transmit and vertical-receive, VV; and horizontal-transmit and horizontal-receive, HH) [17]. The rotating fan beams provide a greater diversity of incident angles and azimuth angle samplings. In our previous work [12], a Bayesian sea ice detection algorithm based on the Geophysical Model Function (GMF) approach was established for the rotation fan beam scatterometer, and the CSCAT 25 km sampling data were applied to validate. This paper investigates the sea ice extent retrieval on a 6.25 km grid using the 12.5 km sampling data from the rotating fan beam scatterometer. CSCAT shares a similar system architecture with WindRad while providing

longer data records (over three years), so we apply the CSCAT 12.5 km sampling data to study the sea ice extent retrieval. In addition, considering that ASCAT operates in the C band and is different from CSCAT in the Ku band, we compare the sea ice extent retrieval results of CSCAT and ASCAT data at a sampling resolution of 12.5 km to investigate the sea ice detection differences between Ku-band and C-band scatterometer data.

The objective of this study is twofold: (1) to investigate the sea ice extent retrieval on a 6.25 km grid using CSCAT 12.5 km sampling data; (2) to evaluate the different capabilities of two types of fan beam scatterometers (Ku-band rotating fan beam CSCAT and C-band fixed fan beam ASCAT) in sea ice detection. A comparison between the sea ice edge and extent on a grid size of 6.25 km of CSCAT and AMSR2 is therefore performed during their overlapping mission period (2020–2022). The sea ice extent on the fine (6.25 km) grid of the CSCAT 12.5 km sampling data is generated by an adapted Bayesian algorithm. A similar comparison is made between ASCAT and AMSR2. A quantitative evaluation between Ku-band CSCAT and C-band ASCAT is also made. Additionally, a comparison of sea ice extent retrieval is conducted on two different sampling resolutions (12.5 km and 25 km) of CSCAT data. Considering the highly dynamic nature of polar sea ice [18], the fine (6.25 km)-grid sea ice extent from CSCAT is beneficial for obtaining local characteristics of polar sea ice distribution and accurate sea ice edges and expanding the ability to link fine-scale sea ice conditions with climate models. As a valuable supplement to the sea ice extent product of AMSR2 on the 6.25 km grid, the results can also be incorporated into the active and passive sea ice detection schemes of AMSR2 to explore any possible improvement in sea ice product.

The paper is organized as follows: Section 2 describes the Bayesian algorithm for the CSCAT 12.5 km sampling data; Section 3 introduces the verification and analysis of the distribution of polar sea ice edges and extents between CSCAT, ASCAT, and AMSR2; and Section 4 summarizes our research findings.

2. Bayesian Algorithm for CSCAT 12.5 km Sampling Data

In scatterometry, GMF is commonly used for ocean wind retrieval, which describes the measured backscatter data as a function of one or more physical parameters. Based on the GMF approach, a Bayesian sea ice detection algorithm for the rotation fan beam scatterometer was established [12]. In this section, an adapted Bayesian algorithm for CSCAT 12.5 km sampling data is introduced. In this section, the CSCAT 12.5 km sampling data are analyzed, and a sea ice GMF model for the CSCAT 12.5 km sampling data is established. We remove duplicate analysis processes and highlight the important calculation procedures and parameter settings of the adapted Bayesian algorithm for the CSCAT 12.5 km sampling data in the paper.

In the Bayesian model, Bayesian statistics are used for decision theory and only assume two types (sea ice and open water) with prior probabilities of $p_0(\text{ice})$ and $p_0(\text{water}) = 1 - p_0(\text{ice})$. Then, the Bayesian theorem can be used to calculate the posterior probability of ice

$$p(\text{ice}|\sigma^0) = \frac{p(\sigma^0|\text{ice})p_0(\text{ice})}{p(\sigma^0|\text{ice})p_0(\text{ice}) + p(\sigma^0|\text{water})(1 - p_0(\text{ice}))} \quad (1)$$

where σ^0 represents backscatter measurements in the CSCAT measurement space [12]. $p(\sigma^0|\text{ice})$ and $p(\sigma^0|\text{water})$ represent the conditional probability of sea ice and open water, respectively.

Using the 12.5 km sampling data of CSCAT as the input and a 55% threshold of the posterior sea ice probability in Equation (1), the Bayesian algorithm updates the CSCAT sea ice mask on each pass and generates a sea ice extent map once a day on a polar stereo grid of 6.25 km. To determine the Bayesian probability of ice, it is necessary to determine the values of $p_0(\text{ice})$, $p(\sigma^0|\text{water})$, and $p(\sigma^0|\text{ice})$, which will be calculated sequentially below.

2.1. $p_0(\text{ice})$

To start, set the prior probability $p_0(\text{ice})$ to a climate value of 0.5 and then update it daily based on the previous day's $p(\sigma^0|\text{ice})$. The $p_0(\text{ice})$ is given by

$$p_0(\text{ice}) = \begin{cases} 0.5, & \text{if } p(\text{ice}|\sigma^0) > 0.30 \\ 0.15, & \text{if } p(\text{ice}|\sigma^0) < 0.30 \end{cases} \quad (2)$$

2.2. $p(\sigma^0|\text{water})$

The conditional probability $p(\sigma^0|\text{water})$ can be calculated by

$$p(\sigma^0|\text{water}) = p(MLE_{\text{wind}}) \quad (3)$$

where MLE (Maximum Likelihood Estimator) is defined as the normalized square distance between backscatter and GMF, and MLE_{wind} refers to the distance for the open water [19].

The value of MLE_{wind} is obtained from the element data named “max_likelihood_est” in CSCAT Level 2B data. For the CSCAT 12.5 km sampling data, the probability distribution of MLE_{wind} can also be fitted as a Gamma distribution [12]. Figure 1 shows two examples of the probability distributions of MLE_{wind} for CSCAT 12.5 km sampling data in 2021. The colored curves in each subgraph represent the histogram contour lines of MLE_{wind} with the same N (number of polarization pairs) but a different Wind Vector Cell (WVC). The bold black curve is the fitted Gamma distribution with shape parameter α and rate parameter β . It is noted that the observed MLE_{wind} distribution is basically consistent with the expected Gamma distribution for both the Arctic and Antarctic regions.

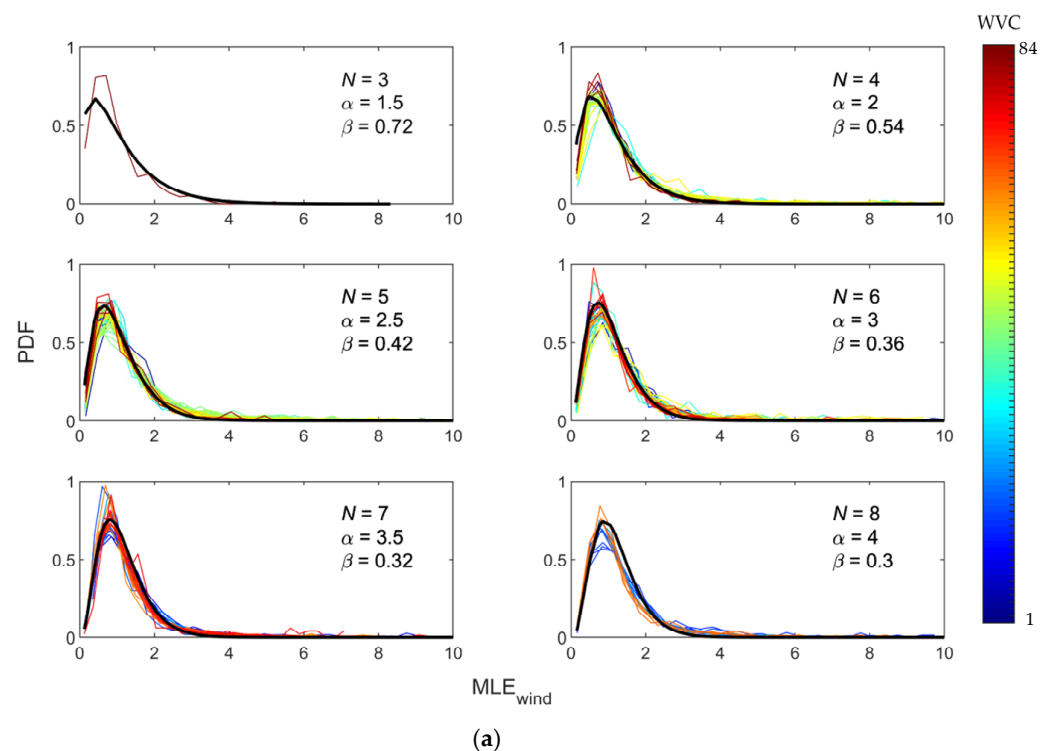


Figure 1. Cont.

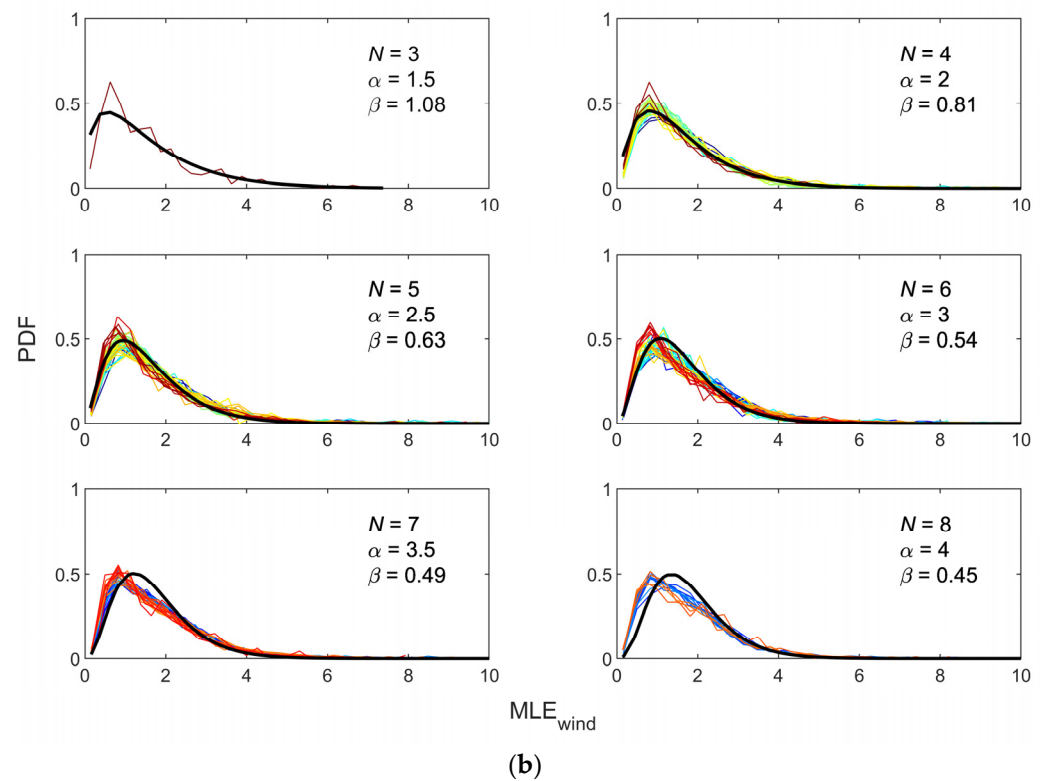


Figure 1. The probability distribution of MLE_{wind} for different N : (a) Arctic region on 10 March 2021; (b) Antarctic region on 10 September 2021. In each subgraph, the colored curves correspond to the histogram contours of MLE_{wind} for different WVCs, and the bold black curve is the fitted Gamma distribution with specific parameters of α and β .

From the available CSCAT 12.5 km sampling data, the data from 2020 to 2022 were chosen as our research scope. The daily CSCAT 12.5 km sampling data were utilized to derive the fitting parameters of MLE_{wind} . We found that the value of α can be generally set to $N/2$, and the value of β varies with different dates of CSCAT 12.5 km data. And a general conclusion on the values of β can be obtained through data analysis, as shown in Table 2. We note that there are different β values for the CSCAT data over the three years. In 2020 and 2021, the value of β varies with different months. That is because CSCAT data have a certain degree of instability, which leads to some differences in the fitting parameters.

Table 2. The values of parameter β applicable to CSCAT 12.5 km sampling data.

Year	Month	$N = 3$	$N = 4$	$N = 5$	$N = 6$	$N = 7$	$N = 8$
2020	1–2	1.22	0.92	0.71	0.61	0.51	0.47
	3	0.53	0.40	0.31	0.26	0.22	0.2
	4–8	0.72	0.54	0.42	0.36	0.3	0.28
	9–12	0.62	0.47	0.36	0.31	0.26	0.24
2021	1–3	0.72	0.54	0.42	0.36	0.32	0.30
	4–5	0.48	0.36	0.28	0.24	0.22	0.20
	6, 8	0.90	0.68	0.52	0.45	0.41	0.38
	7	1.68	1.26	0.98	0.84	0.76	0.7
	9–12	1.08	0.81	0.63	0.54	0.49	0.45
2022	1–12	0.72	0.54	0.42	0.36	0.32	0.3

The final conditional probability $p(\sigma^0 | \text{water})$ can be calculated by

$$p(\sigma^0 | \text{water}) = \text{Ga}\left(\frac{N}{2}, \beta\right) = \frac{1}{\beta^{\frac{N}{2}} \Gamma\left(\frac{N}{2}\right)} MLE_{\text{wind}}^{\frac{N}{2}-1} e^{-MLE_{\text{wind}}/\beta} \quad (4)$$

where the parameter β is detailed in Table 2.

2.3. $p(\sigma^0 | \text{ice})$

Similar to open water, the conditional probability of ice, $p(\sigma^0 | \text{ice})$, is calculated by

$$p(\sigma^0 | \text{ice}) = p(MLE_{\text{ice}}) \quad (5)$$

where MLE_{ice} denotes the normalized square distance between sea ice backscatter and sea ice GMF, which can be expressed as

$$MLE_{\text{ice}} = \sum_i \left[\left(\sigma_i^0 - \sigma_{\text{ice},i}^0 - \mu_i(\sigma_{\text{ice},i}^0) \right) / \text{std}(\sigma_{\text{ice},i}^0) \right]^2, i = 1, \dots, N \quad (6)$$

Here, i is the exponent of one of N (2–8) corresponding to a set of backscatter measurements for each WVC. σ_i^0 is the measured backscatter, $\sigma_{\text{ice},i}^0$ is the corresponding sea ice GMF backscatter, and $\sigma_i^0 - \sigma_{\text{ice},i}^0$ is proven to be a normal distribution with parameters of mean $\mu(\sigma_{\text{ice},i}^0)$ and standard deviation $\text{std}(\sigma_{\text{ice},i}^0)$ [12].

For the CSCAT 12.5 km sampling data, the corresponding sea ice GMF is derived in Section 2.3.1, and then the normal distribution parameters of the distance $\sigma_i^0 - \sigma_{\text{ice},i}^0$ are estimated in Section 2.3.2.

2.3.1. Sea Ice GMF for CSCAT

Considering the backscatter characteristics of sea ice, an empirical sea ice GMF defined in the CSCAT measurement space can be derived, and the expression of the sea ice GMF can be written as

$$\sigma_{\text{ice},HH}^0(\theta) = \text{Slope}(\theta) \times \sigma_{\text{ice},VV}^0(\theta) + \text{Intercept}(\theta) \quad (7)$$

where $\sigma_{\text{ice},HH}^0(\theta)$ and $\sigma_{\text{ice},VV}^0(\theta)$ are HH and VV measurements for the incident angle θ . Different incident angles correspond to different linear functions.

Figure 2 shows the slope and intercept distributions of sea ice GMF for different incident angles, which were obtained from daily CSCAT 12.5 km backscatter data. In the figure, “W”, “S”, “S”, and “F” sequentially represent winter (January to March), spring (April to June), summer (July to September), and fall (October to December). The incident angles of 28–29° and 50–51° were rejected as they lead to significant variations in sea ice GMF for different WVCs. Note that the sea ice GMF model in the winters has the smallest fluctuations, while the sea ice GMF model from mid-spring to early summer has the largest fluctuations, attributed to mixed surface conditions such as sea ice melting. We chose the wintertime data as the most representative data for 100% sea ice concentration and took the average values of the winter parameters as the sea ice GMF model for the CSCAT 12.5 km data.

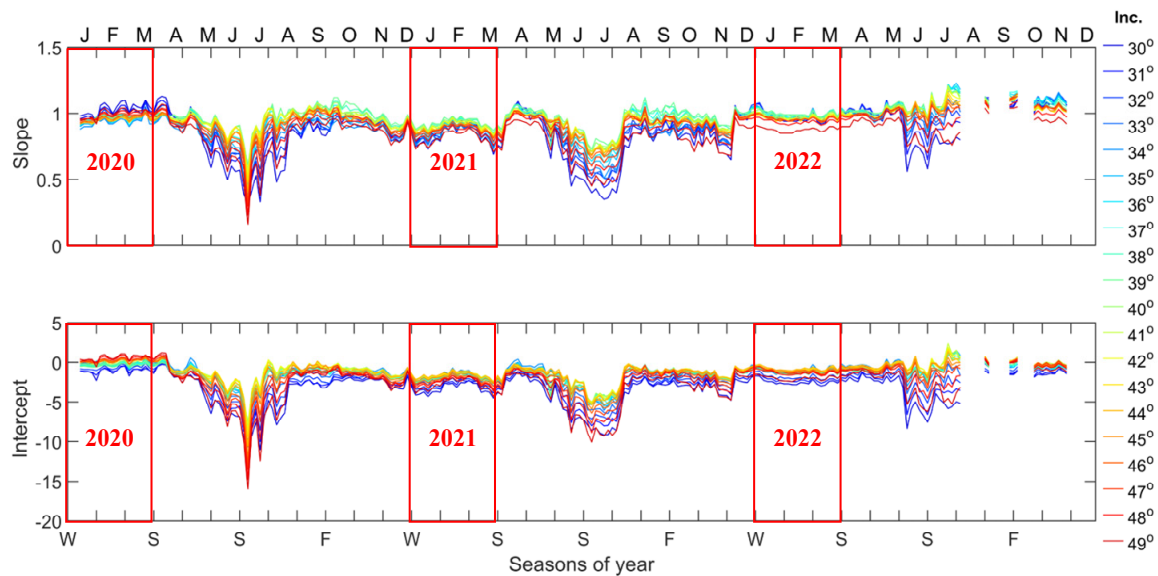


Figure 2. The distribution of sea ice GMF parameters (slope and intercept) at different incident angles for the CSCAT 12.5 km sampling data in the Arctic region.

Figure 3 shows the sea ice GMF of CSCAT 12.5 km sampling data. For ease of reference, the sea ice GMF for CSCAT 25 km sampling data is also illustrated. The slopes of sea ice GMF for CSCAT 12.5 km and 25 km sampling data are basically the same at incident angles of 33–47°, with a maximum slope difference of 0.1 for other incident angles. Overall, the slope of sea ice GMF for CSCAT in 2020 and 2022 is approximately 1, and it is 0.8 in 2021. The deviation between the slopes in 2021 and the other two years is due to calibration issues with the CSCAT data in 2021. Unlike the slope, there is a certain difference in the intercepts between the CSCAT 12.5 km and 25 km sampling data except at an incident angle of 40°. When the incident angle of 40° is used as a reference point, the intercept difference increases with the increased (or decreased) incident angle. In addition, there are significant differences in the intercepts over the past three years.

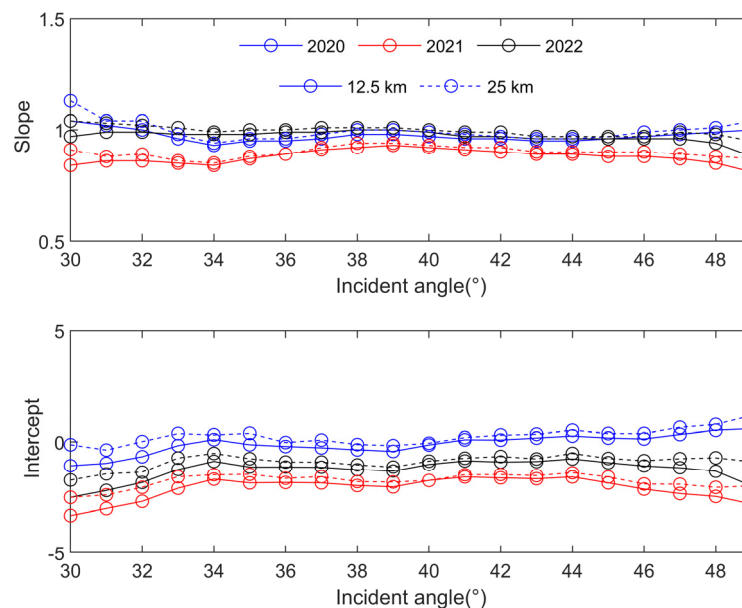


Figure 3. Sea ice GMF model of CSCAT. The curves of different colors represent the results of different years, with solid and dashed lines representing the results from CSCAT 12.5 km and 25 km sampling data, respectively.

2.3.2. Normal Distribution Parameters (μ and std) for $\sigma_i^0 - \sigma_{ice,i}^0$

Using the established sea ice GMF and CSCAT 12.5 km backscatter observations, the backscatter distance from the sea ice to the sea ice GMF, $\sigma_i^0 - \sigma_{ice,i}^0$, can be calculated, and the histogram distribution of the distances approaches the normal distribution. The detailed analysis process is similar to our previous work [12], so this paper does not elaborate further. Figure 4 shows the normal distribution parameter estimation results for different incident angles of CSCAT 12.5 km sampling data from 2020 to 2022. Note that the values of μ corresponding to three different years are similar. The values are almost 0 dB at incident angles of 36–43°, and the variation range is ± 0.2 dB for different incident angles. The std value gradually decreases with an increase in incident angle, and the corresponding std value in 2020 is relatively smaller than those in 2021 and 2022. The certain difference between std in 2020 and 2021 (or 2022) may be caused by the instability of CSCAT data in 2021 and 2022.

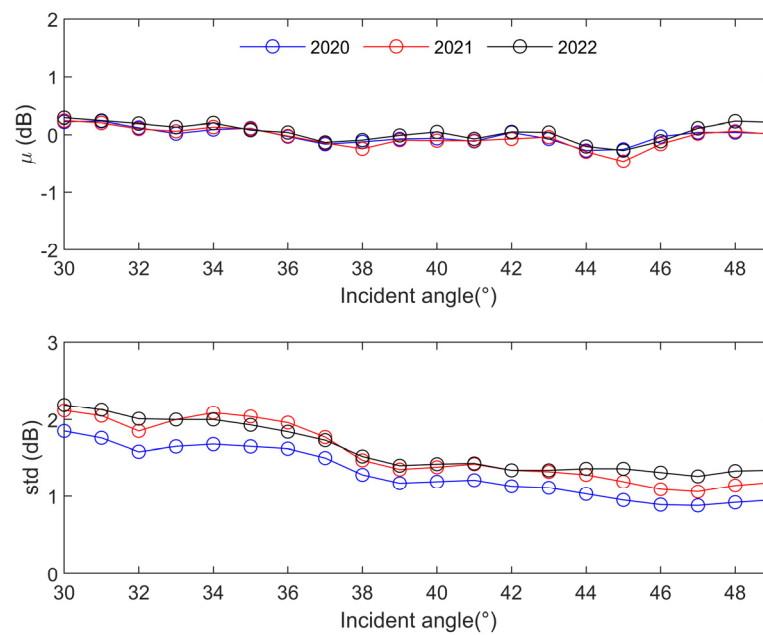


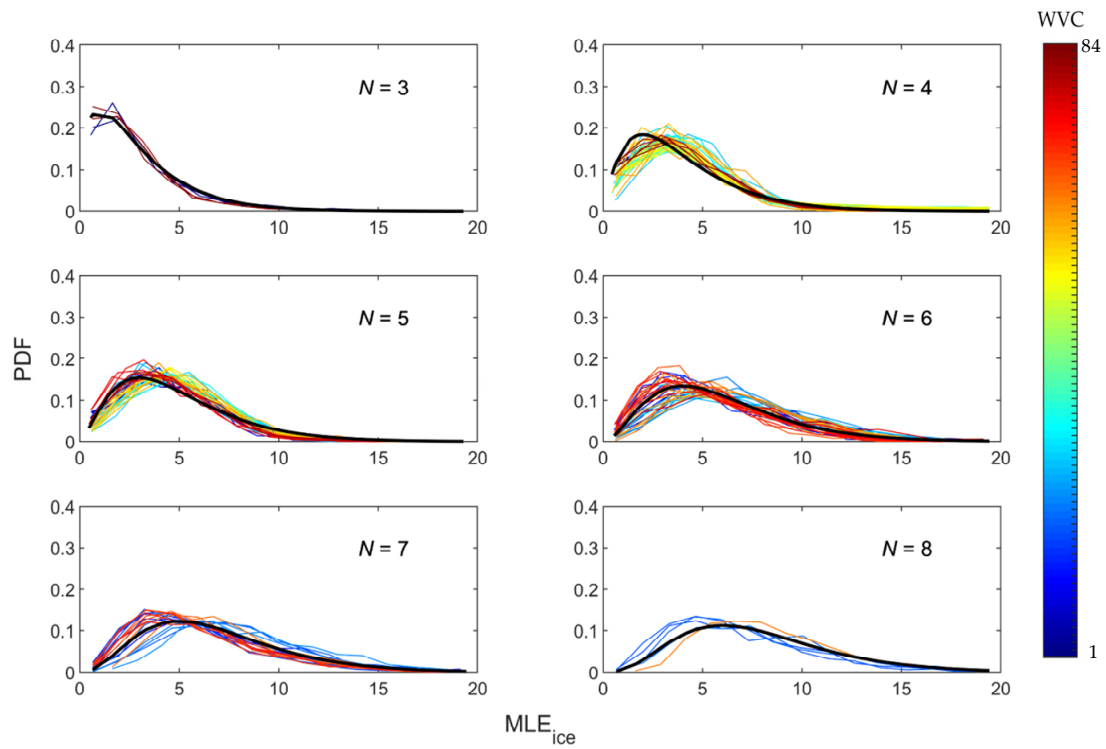
Figure 4. Normal distribution parameters (mean μ and standard deviation std) of the distribution of $\sigma_i^0 - \sigma_{ice,i}^0$ for CSCAT 12.5 km sampling data. Different colored curves represent the results of different years.

2.3.3. $p(MLE_{ice})$

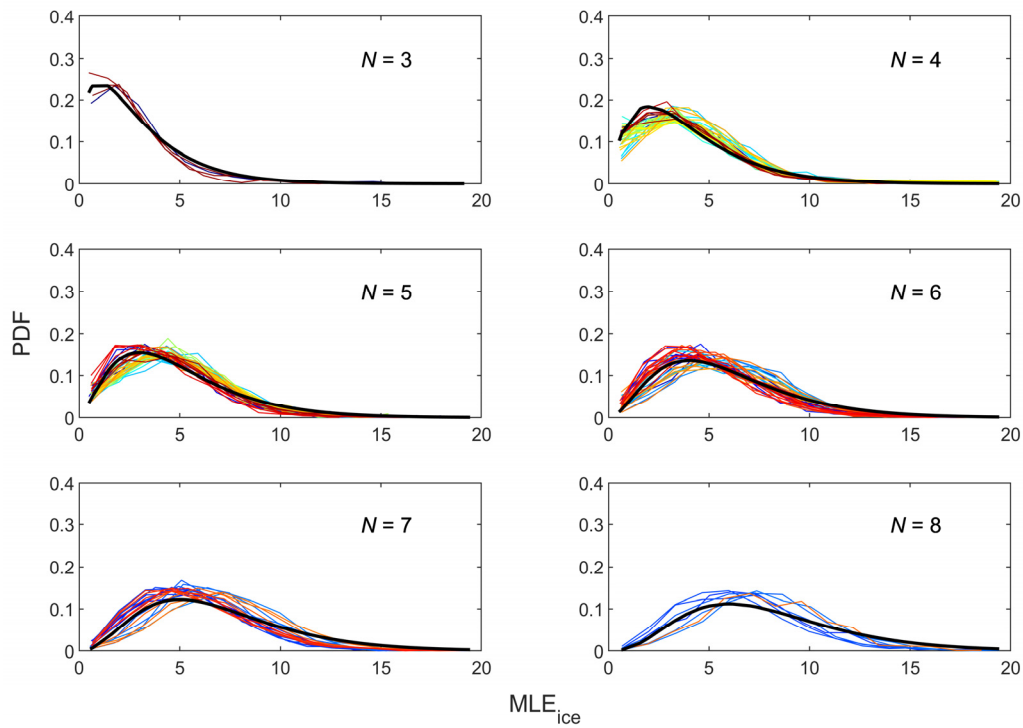
As mentioned above, the distribution of the normalized distance of $\sigma_i^0 - \sigma_{ice,i}^0$ is approximately a standard normal distribution. Then, MLE_{ice} follows a chi square distribution with N degrees of freedom, which can be written as

$$p(MLE_{ice}) = \chi_N^2(MLE_{ice}) = \frac{1}{2^{N/2}\Gamma(N/2)} MLE_{ice}^{N/2-1} e^{-MLE_{ice}/2} \quad (8)$$

Figure 5 shows an example of the probability distribution of the MLE_{ice} . Here, one day’s data are used to evaluate the histogram contours of MLE_{ice} for all WVCs with the same observation pair N . For each subgraph, the colored curves represent the contours for different WVCs, and the bold black one is the corresponding fitted chi square distribution. The statistical distribution of MLE_{ice} generally follows the chi square distribution with parameter N for both the Arctic and Antarctic regions.



(a)



(b)

Figure 5. The probability distribution of MLE_{ice} for different N : (a) Arctic region on 10 March 2021; (b) Antarctic region on 10 September 2021. In each subgraph, the colored curves correspond to the histogram contours of MLE_{ice} for different WVC, and the bold black curve is the fitted chi square distribution with N degrees.

3. Results

By utilizing the Bayesian algorithm described in Section 2, the sea ice extent of CSCAT 12.5 km sampling data is generated daily on a high-resolution grid with a pixel spacing of 6.25 km. In this section, the sea ice extent maps generated from CSCAT 12.5 km sampling data are validated and analyzed.

In order to evaluate the capability of CSCAT 12.5 km sampling data in mapping polar sea ice extents and investigate the differences in sea ice detection of Ku-band and C-band scatterometers at a sampling resolution of 12.5 km, comparisons are made with sea ice extent maps obtained by AMSR2, ASCAT onboard MetOp-C (ASCAT-C) 12.5 km sampling data, and CSCAT 25 km sampling data. The sea ice extent maps here are all in polar stereo projections of the National Snow and Ice Data Center (NSIDC) [20]. For AMSR2, the sea ice extent is obtained by setting a 15% threshold onto a sea ice concentration product generated by the ASI ice concentration algorithm [21]. The sea ice concentration product is provided by the University of Bremen and has two different grid sizes (3.125 km and 6.25 km) [22]. In our study, the sea ice concentration product with a grid size of 6.25 km is used. For ASCAT, the sea ice extent maps are generated through an ice screening process based on the Bayesian algorithm detailed in [9]. The grid size of the sea ice extent maps is the same as the resolution of the corresponding sampling data. For the ASCAT-C 12.5 km sampling data, the sea ice extent maps are on the 12.5 km grid [23]. The sea ice extent maps of the CSCAT 25 km sampling data are located on the 12.5 km grid [12].

Figure 6 shows two ice-masked image samples of the CSCAT 12.5 km sampling data when the sea ice extents in the Arctic and Antarctic regions approach their maximum values. The corresponding sea ice edges are represented as red outlines. The sea ice edge estimates of AMSR2 at 15% sea ice concentration (black contours), ASCAT-C 12.5 km sampling data retrieved sea ice edges (green contours), and CSCAT 25 km sampling data-derived sea ice edges (blue contours) are superimposed on each frame as well. For the convenience of sea ice edge comparison, the sea ice extent maps of ASCAT-C 12.5 km sampling data and CSCAT 25 km sampling data are interpolated into the 6.25 km grid. It is observed that the sea ice edges of CSCAT 12.5 km sampling data usually track the edges of AMSR2 at 15% sea ice concentration and CSCAT 25 km sampling data, and there are some differences from the edges of ASCAT-C.

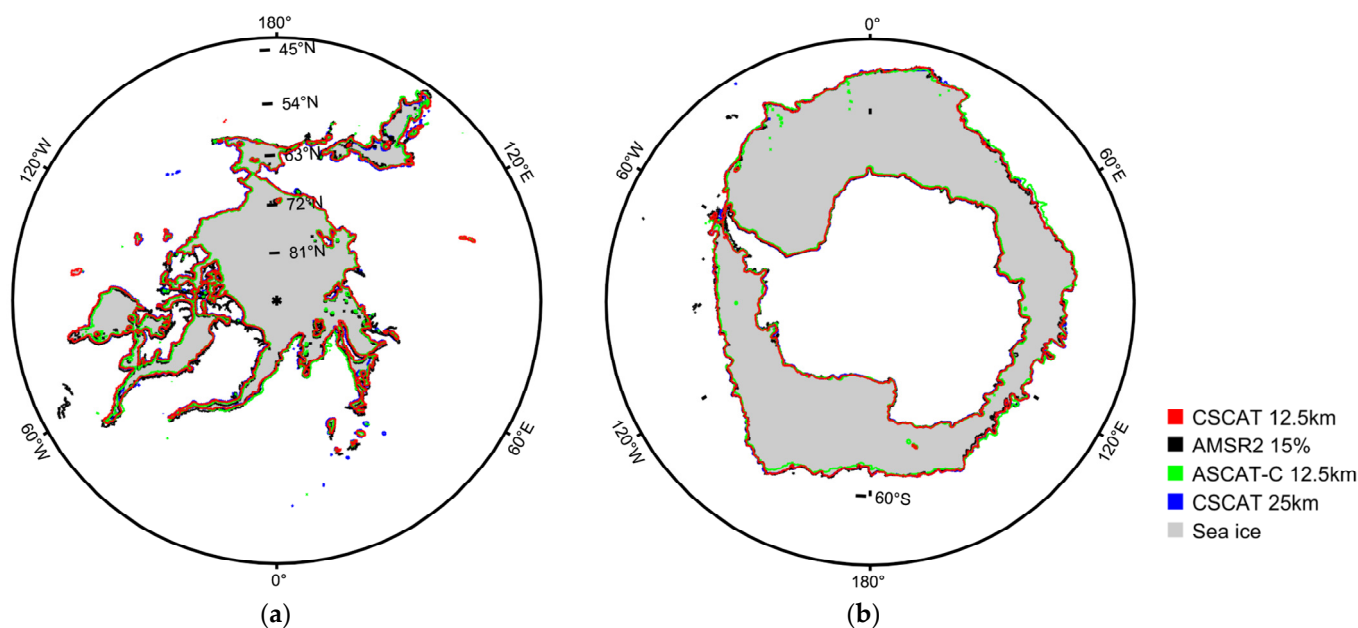


Figure 6. Sea ice extent maps of CSCAT 12.5 km sampling data: (a) Arctic region on 1 March 2021; (b) Antarctic region on 10 September 2021. The sea ice edge estimates are superimposed on each frame, and different colors represent the resulting sea ice edges of different data.

Additionally, Figure 7 shows a quantitative comparison of the Euclidean distance (ED) of the sea ice edges in Figure 6 [24]. In the figure, the spatial and statistical distributions of sea ice edge ED between CSCAT 12.5 km data and AMSR2 at 15% sea ice concentration, ASCAT-C 12.5 km data and AMSR2 at 15% sea ice concentration, CSCAT 12.5 km data and ASCAT-C 12.5 km data, and CSCAT 12.5 km data and CSCAT 25 km data are illustrated, respectively. It is noted that the sea ice edges of CSCAT 12.5 km data and AMSR2 at 15% sea ice concentration are highly correlated and match each other within the mean ED of approximately 1 pixel (6.25 km) and 1.5 pixels (9.4 km) in the Arctic and Antarctic regions accordingly. For the sea ice edge ED between ASCAT-C 12.5 km data and AMSR2 at 15% sea ice concentration, the larger ED values are distributed at the junction of ice and land. Meanwhile, for the Antarctic region, the ASCAT-C sea ice edge differs significantly from that of AMSR2 at 15% sea ice concentration when compared to the results of CSCAT 12.5 km data versus AMSR2 at 15% sea ice concentration. That is because the sea ice edge area usually corresponds to the area with lower sea ice concentration, and the sensitivity of C-band and Ku-band scatterometry to sea ice with low sea ice concentration is different. Due to the short wavelength of the Ku band, the backscatter contrast between sea ice and open water is higher than that of the C band. Ku-band scatterometry also shows lower penetration and more sensitivity to the sea ice [25]. There are large proportions of significant differences ($ED > 3$ pixels) occurring at the sea ice edges between CSCAT 12.5 km data and ASCAT-C 12.5 km data. Furthermore, for the Arctic region, the mean ED value of the sea ice edges between CSCAT 12.5 km and 25 km data is the largest at approximately 2.4 pixels (15 km). In the Antarctic region, the ED value is around 1.8 pixels (11 km). It is obvious that large ED values appear at the junction of ice and land for both Arctic and Antarctic regions. The different sampling resolutions of CSCAT data can lead to different sea ice edges, especially for the Arctic region.

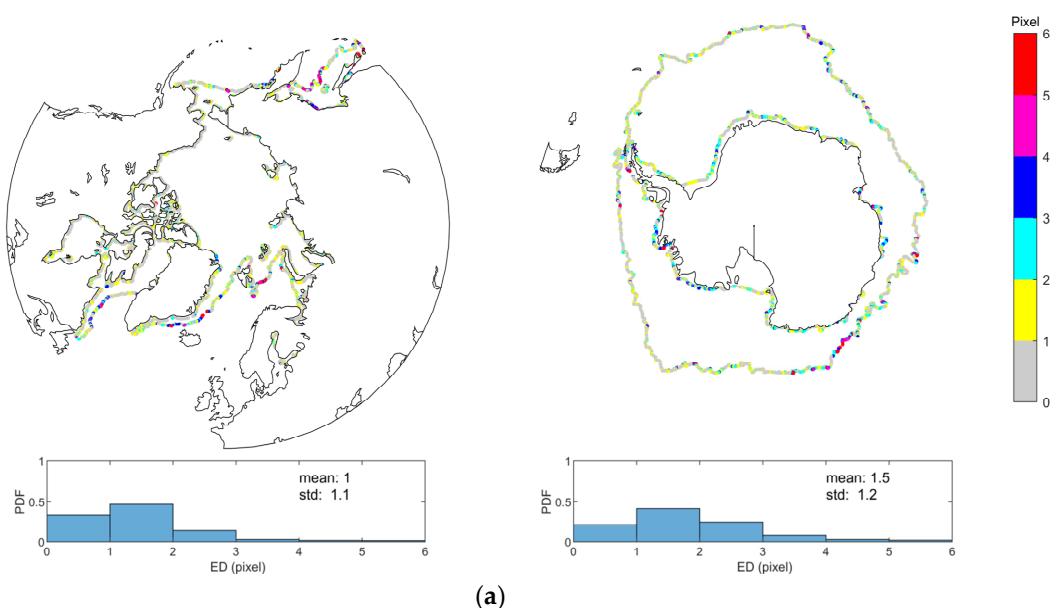


Figure 7. Cont.

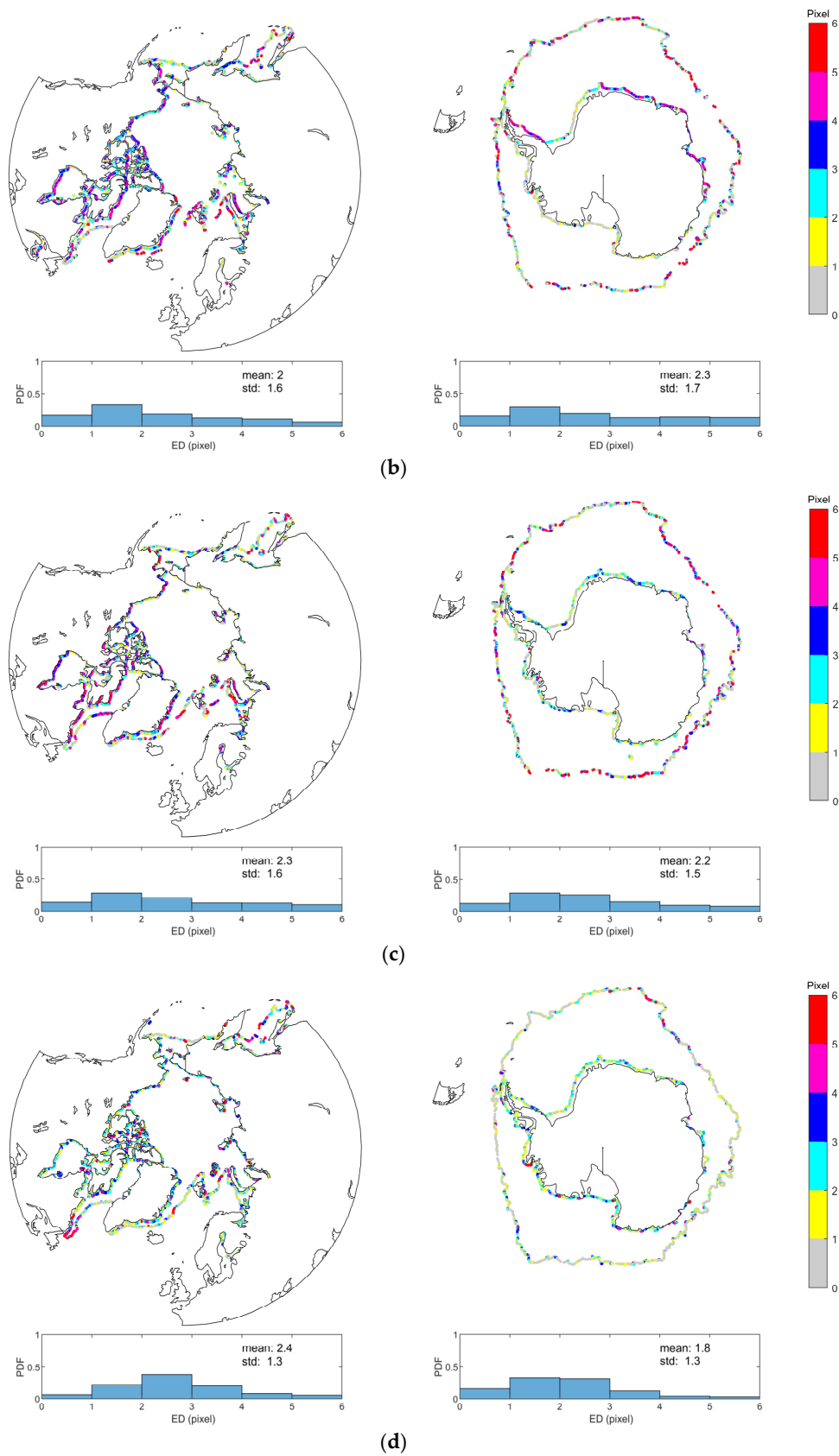


Figure 7. The spatial and statistical distributions of sea ice edge ED correspond to Figure 6: (a) CSCAT 12.5 km vs. AMSR2 15%; (b) ASCAT-C 12.5 km vs. AMSR2 15%; (c) CSCAT 12.5 km vs. ASCAT-C 12.5 km; (d) CSCAT 12.5 km vs. CSCAT 25 km.

Again, the monthly average ice edge ED distributions of (a) CSCAT 12.5 km data versus AMSR2 at 15% sea ice concentration, (b) ASCAT-C 12.5 km data versus AMSR2 at 15% sea ice concentration, (c) CSCAT 12.5 km data versus ASCAT-C 12.5 km data, and (d) CSCAT 12.5 km data versus CSCAT 25 km data are plotted in Figure 8. We notice that the sea ice edges of CSCAT 12.5 km data and AMSR2 at 15% sea ice concentration match the best, with a mean edge ED of around 7 km and 10 km in the Arctic and Antarctic regions. In the Arctic region, the mean and standard deviation of the sea ice edge ED increase during the summer period (from August to October). The reason for this phenomenon is that the sea ice concentration derived from the passive microwave brightness temperatures is affected by the surface wetness during the melt season, typically underestimating the summer sea ice concentration [26]. Furthermore, the fluctuations in the Antarctic region are less than those of the Arctic region. That is because the sea ice in the Arctic region is far more sensitive to climate change than that in the Antarctic region [27]. Meanwhile, the sea ice edges of ASCAT 12.5 km data and AMSR2 at 15% sea ice concentration match each other within mean EDs of about 12.5 km and 15 km in the Arctic and Antarctic regions. These results indicate that CSCAT 12.5 km data can provide a better estimation of sea ice edges than ASCAT 12.5 km data. The reason is that the shorter wavelength of the Ku band can provide greater ice/water contrast but reduced penetration and greater atmospheric sensitivity than the C band [25]. Additionally, the sea ice edge ED values between CSCAT 12.5 km data and ASCAT C 12.5 km data are calculated, and the results show the mean ED value in the Arctic region is about 14 km for 2020 and 2021 and 12.5 km for 2022. In the Antarctic region, the mean ED values in different months are similar, and the mean ED distributions over the three years almost overlap. The mean ED is about 14 km. Unlike the Antarctic region, there is a significant fluctuation of ED values from July to October in the Arctic region. Moreover, the sea ice edge ED between CSCAT 12.5 km and 25 km data is approximately 13 km in the Arctic region. In the Antarctic region, the corresponding ED is about 10 km for 2020 and 2022, and 11 km for 2021.

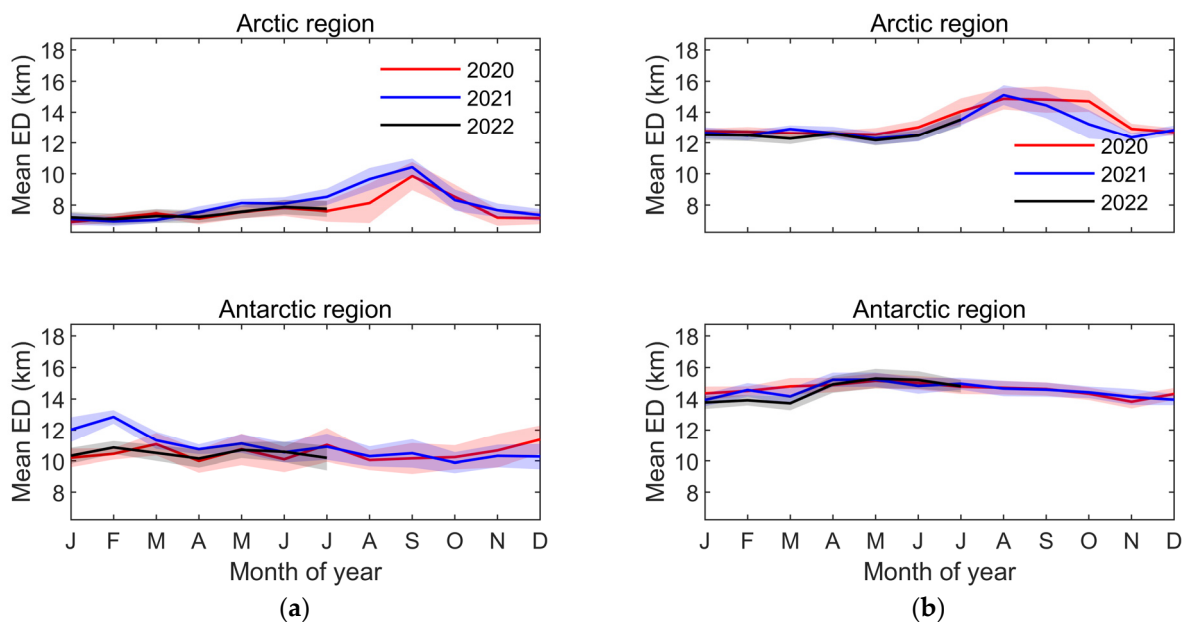


Figure 8. Cont.

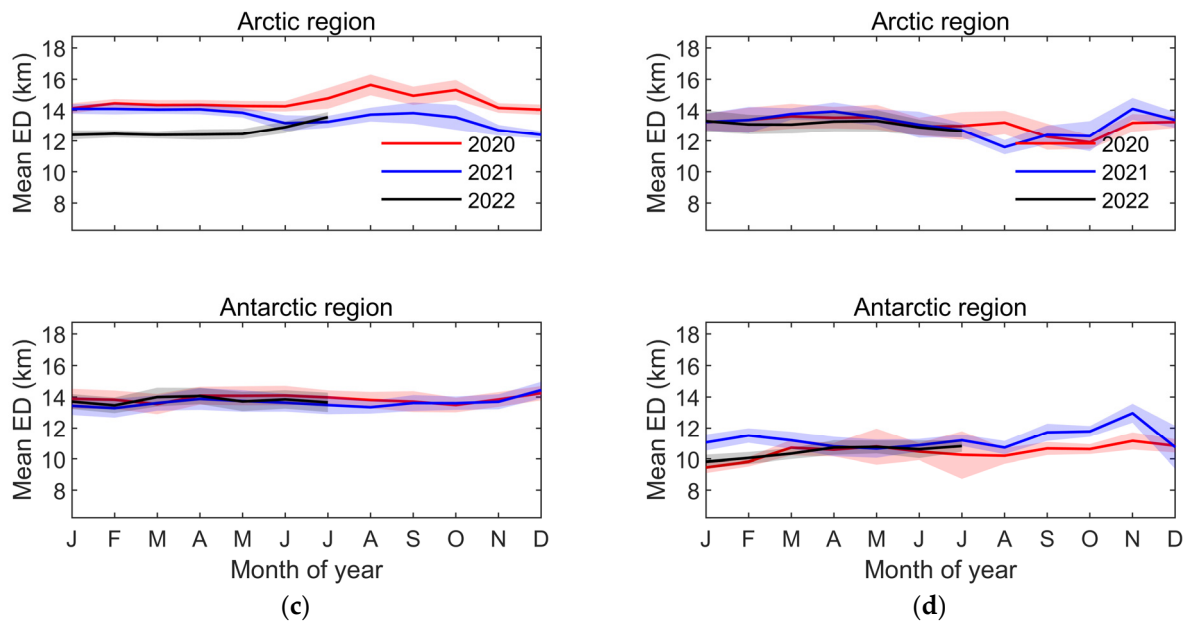


Figure 8. Monthly average sea ice edge ED distributions for the Arctic and Antarctic regions: (a) CSCAT 12.5 km vs. AMSR2 15%; (b) ASCAT-C 12.5 km vs. AMSR2 15%; (c) CSCAT 12.5 km vs. ASCAT-C 12.5 km; (d) CSCAT 12.5 km vs. CSCAT 25 km. The different colored curves represent the results for different years, and the shadow of each curve represents the standard deviation of ED.

As shown in Figure 8, the distribution of ED in the Arctic region exhibits significant seasonal fluctuations, especially in summer. And it can also be seen from Figure 6 that the increase in the proportion of large EDs ($ED > 3$ pixels) leads to a larger mean value of the ED. Therefore, we analyze the spatial distribution of EDs larger than 3 pixels in the Arctic region from May to October 2020. We notice that the large ED values between CSCAT 12.5 km data and AMSR2 at 15% sea ice concentration data are mainly located at the sea ice edge area near Greenland. Furthermore, there is a significant distribution of large EDs at the sea ice edge in September. That is because large uncertainties have been revealed in passive microwave sea ice extent products in the marginal ice zone during the melting season [28]. By comparing Figure 9a,b, it is noted that the ED values between ASCAT-C 12.5 km data and AMSR2 at 15% sea ice concentration data are larger. It indicates that the Ku-band backscatter measurements have a better performance in sea ice monitoring compared to the C band. At the same time, we also noticed that there is an extensive distribution of large ED values at the junction of land and sea. Furthermore, it can be seen in Figure 9c,d that large EDs are mainly distributed at the junction of sea and land.

The evolution of the sea ice extent of CSCAT 12.5 km sampling data is also studied. The results are compared with the corresponding trends derived from AMSR2 and ASCAT. The pixels marked as ice in the sea ice extent map are summed up every day, and the total extent is calculated using the pixel size of polar stereo projection. The pixel sizes of sea ice extent maps are 6.25 km for CSCAT 12.5 km sampling data and AMSR2 15% sea ice concentration, and 12.5 km for ASCAT-C 12.5 km data and CSCAT 25 km sampling data. The total sea ice extent results from 2020 to 2022 are shown in Figure 10. These plots illustrate the overall seasonal and annual changes in sea ice extent over a three-year period. We find that the agreement between CSCAT 12.5 km data and AMSR2 15% sea ice concentration derived sea ice extent is good throughout the year. There is a significant difference between the 12.5 km and 25 km sampling data of CSCAT, and the 25 km data can lead to overestimation of the sea ice extent. In the Arctic region, the sea ice extent in the CSCAT 12.5 km data and the ASCAT-C 12.5 km data is similar in summer and autumn, but there are certain differences in winter and early spring. That is because there is a large amount of land and sea areas in the Arctic region, and the 6.25 km gridded sea ice extent map of CSCAT 12.5 km data is more conducive to calculating the sea ice extent over these

areas compared to the 12.5 km gridded sea ice extent map obtained from ASCAT-C 12.5 km data. In addition, the higher atmosphere sensitivity of the Ku-band frequency compared to the C-band frequency can also lead to the differences between them. In the Antarctic region, the ice extent of ASCAT 12.5 km data shows the closest correlation to the result of CSCAT 12.5 km. The reason is that the sea ice in the Antarctic region is very stable throughout the year.

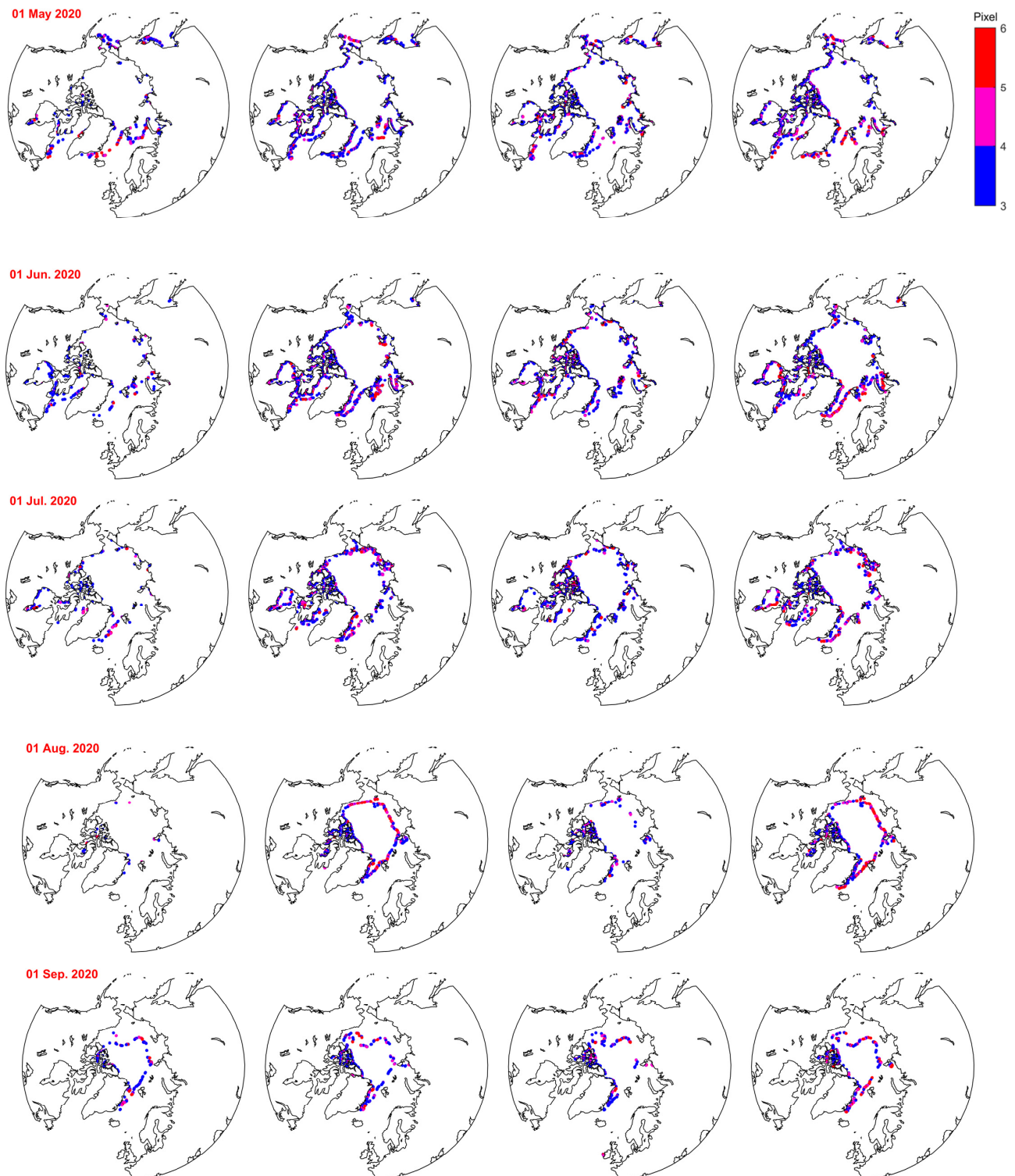


Figure 9. Cont.

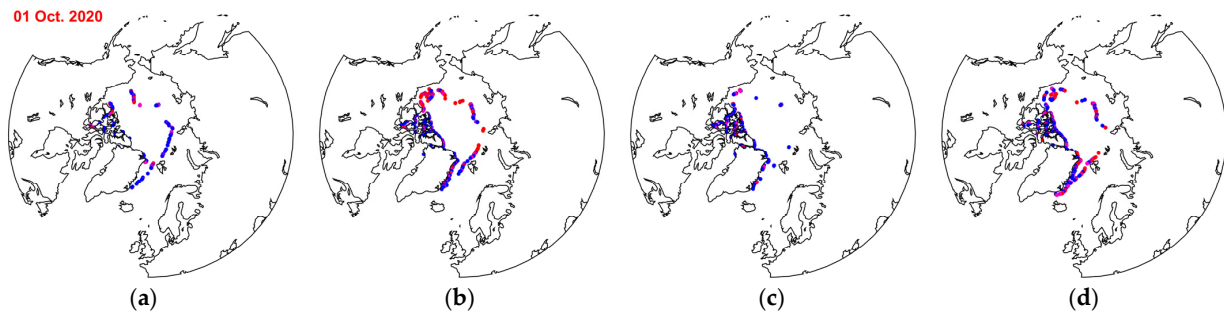


Figure 9. The spatial distribution of EDs larger than 3 pixels in the Arctic region from May to October 2020: (a) CSCAT 12.5 km vs. AMSR2 15%; (b) ASCAT-C 12.5 km vs. AMSR2 15%; (c) CSCAT 12.5 km vs. ASCAT-C 12.5 km; (d) CSCAT 12.5 km vs. CSCAT 25 km. Each row in the figure represents the same date but different ED comparisons, and each column in the figure represents the same ED comparison but different dates.

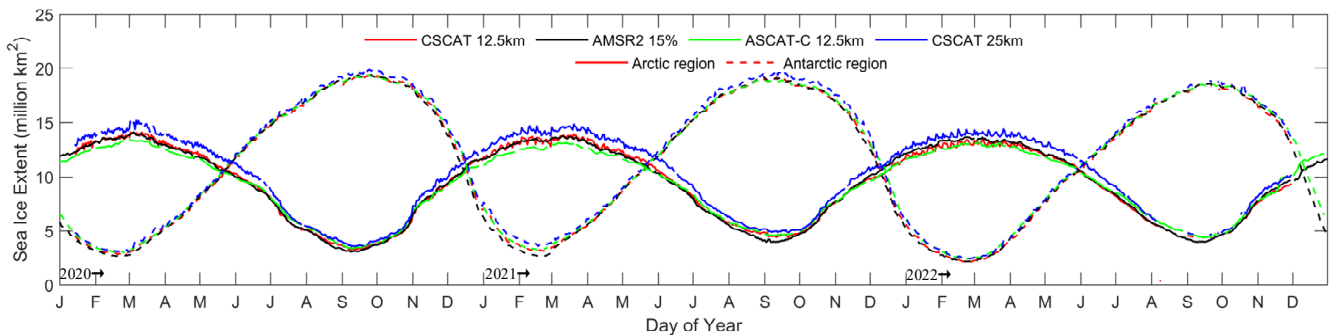


Figure 10. Daily sea ice extent of CSCAT 12.5 sampling data (red), AMSR2 at 15% sea ice concentration (black), ASCAT-C 12.5 sampling data (green), and CSCAT 25 sampling data (blue) during 2020–2022, where the solid and dashed lines represent the Arctic and Antarctic regions.

Figure 11 compares the monthly average sea ice extent differences between CSCAT 12.5 km data and AMSR2 at 15% sea ice concentration, ASCAT-C 12.5 km data and AMSR2 at 15% sea ice concentration, CSCAT 12.5 km data and ASCAT-C 12.5 km data, and CSCAT 12.5 km data and CSCAT 25 km data. The mean and standard deviation of the sea ice extent differences for each month over three years are presented in the figure. We observe that the maximum difference between the CSCAT 12.5 km data and AMSR2 records occurs during rapid sea ice advance or retreat. The difference is within 0.25 million km² for 2020 and 0.5 million km² for 2021 and 2022. The instability of CSCAT data in 2021 and 2022 leads to the larger sea ice extent difference. The sea ice extent difference in the Antarctic region is smaller than that in the Arctic region, while the monthly average of ice extent between ASCAT-C 12.5 km data and AMSR2 records shows a larger difference. This further indicates that the Ku-band scatterometer performs better than the C-band scatterometer in estimating sea ice extent. Furthermore, the sea ice extent difference between CSCAT 12.5 km data and ASCAT-C 12.5 km data is small except for January to May 2020 and 2021 for the Arctic region. This may be due to the different grid sizes of them and the varying sensitivity of different detection frequencies to the presence of sea ice. In addition, in the Antarctic region, the sea ice extent difference between CSCAT 12.5 km data and ASCAT-C 12.5 km data is almost negative, indicating that ASCAT has a slightly larger estimated value compared to CSCAT, and the overestimation is generally less than 0.25 million km². Moreover, compared with the CSCAT 12.5 km sampling data, the overestimation of sea ice extent retrieved from the CSCAT 25 km sampling data is basically 0.3–1.0 million km².

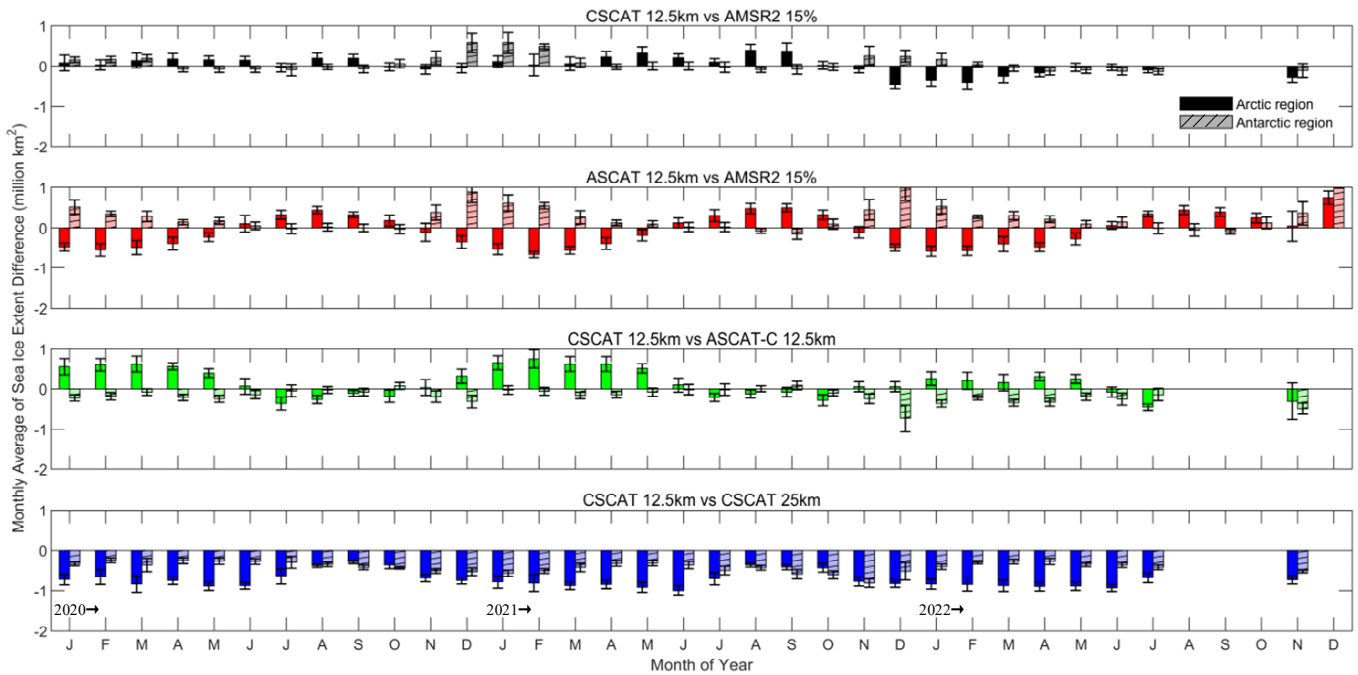


Figure 11. Monthly average of sea ice extent difference among CSCAT 12.5 km sampling data, AMSR2 at 15% sea ice concentration, ASCAT-C 12.5 km sampling data, and CSCAT 25 km sampling data.

To further illustrate the comparison of the sea ice extent between the scatterometer 12.5 km sampling data and radiometer sea ice concentration data, the seasonal average differences in polar sea ice extent between CSCAT/ASCAT-C 12.5 km data and AMSR2 at 15% sea ice concentration data are shown in Figure 12. Due to the lack of data for the second half of 2022 from CSCAT, the chart only shows the results of 2020 and 2021. It is worth noting that the sea ice extent difference is relatively low in autumn and winter but higher in spring and summer, and the sensitivity of passive microwave (AMSR2) products to melting sea ice conditions is lower than that of the scatterometer.

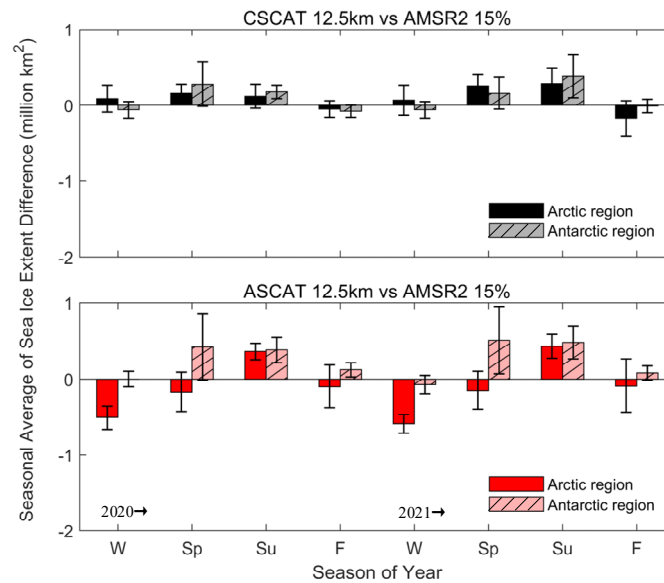


Figure 12. Seasonal average of sea ice extent difference between CSCAT/ASCAT 12.5 km sampling data and AMSR2 at 15% sea ice concentration data from 2020 to 2021.

4. Conclusions

The high-resolution (12.5 km) sampling data of the fan beam scatterometers provides the possibility to retrieve large-scale sea ice extents on a 6.25 km grid. Considering the highly dynamic nature of polar sea ice, the fine (6.25 km)-gridded sea ice extent is beneficial for characterizing the local distribution of sea ice, obtaining accurate sea ice edges, and expanding the ability to link fine-scale sea ice conditions with climate models. This paper investigates the sea ice extent retrieval on a 6.25 km grid using the CSCAT 12.5 km sampling data. Meanwhile, the sea ice detection capabilities of the Ku-band rotating fan beam CSCAT and C-band fixed fan beam ASCAT are evaluated. Using the CSCAT 12.5 km sampling data, the sea ice extent map on the 6.25 km grid is generated by an adapted Bayesian algorithm. In this paper, the CSCAT 12.5 km sampling data are analyzed, a corresponding sea ice GMF model is established, and the important calculation procedures and parameter settings of the adapted Bayesian algorithm for CSCAT 12.5 km sampling data are elaborated on. A comparison of the sea ice edge and extent among CSCAT 12.5 km sampling data, AMSR2, ASCAT-C 12.5 km sampling data, and CSCAT 25 km sampling data is performed during their overlapping mission period (2020–2022).

The results show that the sea ice extent of CSCAT 12.5 km sampling data is consistent with the sea ice extent of AMSR2 at 15% sea ice concentration. The sea ice edge accuracy is about 7 km and 10 km for the Arctic and Antarctic regions, and the difference in sea ice extent is 0.25 million km² for 2020 and 0.5 million km² for 2021 and 2022. The sea ice extent difference in the Antarctic region is smaller than that in the Arctic region. The sea ice edge ED and extent between ASCAT 12.5 km sampling data and AMSR2 at 15% sea ice concentration are calculated. The sea ice edge EDs between them are 12.5 km and 15 km for the Arctic and Antarctic regions, respectively. The sea ice extent differences between them are larger than those of CSCAT 12.5 km sampling data and AMSR2 at 15% sea ice concentration. These indicate that CSCAT 12.5 km sampling data show a better estimation of polar sea ice extents than ASCAT 12.5 km sampling data. This may be due to the fact that backscatter observations in the Ku band can present a larger ice/water contrast than those in the C band. The sea ice edge ED between CSCAT 12.5 km sampling data and ASCAT C 12.5 km sampling data is 14 km in 2020 and 2021 and 12.5 km in 2022 for the Arctic region, and 14 km for the Antarctic region. In the Arctic region, the corresponding sea ice extent difference between them is small except for January to May in 2020 and 2021. That is because of their different grid sizes and the different sensitivities to the presence of sea ice. The sea ice extent difference in the Antarctic region is generally less than 0.25 million km². Moreover, the derived sea ice extents from the two different (12.5 km and 25 km) sampling data of CSCAT show some deviations. The corresponding sea ice edge ED is about 13 km for the Arctic region, and 10 km in 2020 and 2022 and 12 km in 2021 for the Antarctic region. The sea ice extent of the CSCAT 25 km sampling data is usually overestimated, and the overestimation is about 0.3–1.0 million km².

Overall, compared to the sea ice extent product of AMSR2, the sea ice extent retrieved from the CSCAT 12.5 km sampling data has better consistency than the ASCAT 12.5 km sampling data. The sea ice extent of the CSCAT 25 km sampling data is overestimated compared to that of the CSCAT 12.5 km sampling data. There is a significant difference in the sea ice extent between the 12.5 km and 25 km sampling data of CSCAT, and the 25 km data overestimate the sea ice extent. The sea ice extent on the 6.25 km grid of the 12.5 km sampling data from a Ku-band rotating fan beam scatterometer can provide a valuable independent description of the fine-scale state of polar sea ice cover.

Author Contributions: Conceptualization, L.L. and X.D.; methodology, L.L. and W.L.; software, L.L.; validation, L.L.; formal analysis, L.L.; investigation, L.L.; resources, S.L.; data curation, L.L.; writing—original draft preparation, L.L. and L.Y.; writing—review and editing, L.L. and W.L.; visualization, L.L.; supervision, X.D.; project administration, S.L. and L.L.; funding acquisition, L.L. All authors have read and agreed to the published version of the manuscript.

Funding: This research is funded by the National Natural Science Foundation of China (Grant No. 41806209) and Project 2023CFO017 supported by Key Laboratory of Space Ocean Remote Sensing and Application, MNR.

Data Availability Statement: The CSCAT scientific product used in the study is available at the NSOAS website: <https://osdds.nsoas.org.cn/> (accessed on 15 October 2023). The AMSR2 dataset is available at <https://data.seaice.uni-bremen.de/databrowser/#p=sic> (accessed on 8 November 2023) and the ASCAT-C dataset is available at <https://osi-saf.eumetsat.int/products/osi-104-c> (accessed on 2 December 2023).

Acknowledgments: We acknowledge the support of the NSOAS and CFOSAT team in providing the data, status and mission information. The passive microwave datasets provided by the University of Bremen and ASCAT-C datasets provided by EUMETSAT Ocean and Sea Ice SAF are much appreciated.

Conflicts of Interest: The authors declare no conflicts of interest.

References

1. Cartwright, J.; Fraser, A.D.; Porter-Smith, R. Polar maps of C-band backscatter parameters from the Advanced Scatterometer. *Earth Syst. Sci. Data* **2022**, *14*, 479–490. [[CrossRef](#)]
2. Sandven, S.; Spreen, G.; Heygster, G.; Girard-Ardhuin, F.; Farrell, S.L.; Dierking, W.; Allard, R.A. Sea Ice Remote Sensing—Recent Developments in Methods and Climate Data Sets. *Surv. Geophys.* **2023**, *44*, 1653–1689. [[CrossRef](#)]
3. OSI-SAF Sea-Ice-Products. Available online: <https://osi-saf.eumetsat.int/products/sea-ice-products> (accessed on 10 December 2023).
4. AMSR-E/AMSR2 Unified L3 Daily 12.5 Km Brightness Temperatures, Sea Ice Concentration, Motion & Snow Depth Polar Grids V001. Version 1. Available online: <https://catalog.data.gov/dataset/amr-e-amr2-unified-l3-daily-12-5-km-brightness-temperatures-sea-ice-concentration-motion> (accessed on 7 December 2023).
5. Melsheimer, C.; Spreen, G. *AMSR2 ASI Sea Ice Concentration Data, Arctic, Version 5.4 (NetCDF) (January 2020–January 2022)*; PANGAEA: Bremen, Germany, 2019.
6. Ivanova, N.; Pedersen, L.T.; Tonboe, R.T.; Kern, S.; Heygster, G.; Lavergne, T.; Sørensen, A.; Saldo, R.; Dybkjær, G.; Brucker, L.; et al. Inter-comparison and evaluation of sea ice algorithms: Towards further identification of challenges and optimal approach using passive microwave observations. *Cryosphere* **2015**, *9*, 1797–1817. [[CrossRef](#)]
7. Keller, M.R.; Gifford, C.M.; Winstead, N.S.; Walton, W.C.; Dietz, J.E. Active/Passive Multiple Polarization Sea Ice Detection During Initial Freeze-Up. *IEEE Trans. Geosci. Remote Sens.* **2021**, *59*, 5434–5448. [[CrossRef](#)]
8. Rivas, M.B.; Stoffelen, A. New Bayesian Algorithm for Sea Ice Detection With QuikSCAT. *IEEE Trans. Geosci. Remote Sens.* **2011**, *49*, 1894–1901. [[CrossRef](#)]
9. Rivas, M.B.; Verspeek, J.; Verhoef, A.; Stoffelen, A. Bayesian Sea Ice Detection With the Advanced Scatterometer ASCAT. *IEEE Trans. Geosci. Remote Sens.* **2012**, *50*, 2649–2657. [[CrossRef](#)]
10. Otosaka, I.; Rivas, M.B.; Stoffelen, A. Bayesian Sea Ice Detection With the ERS Scatterometer and Sea Ice Backscatter Model at C-Band. *IEEE Trans. Geosci. Remote Sens.* **2018**, *56*, 2248–2254. [[CrossRef](#)]
11. Li, Z.; Verhoef, A.; Stoffelen, A. Bayesian Sea Ice Detection Algorithm for CFOSAT. *Remote Sens.* **2022**, *14*, 3569. [[CrossRef](#)]
12. Liu, L.; Dong, X.; Lin, W.; Lang, S. Polar Sea Ice Detection Using a Rotating Fan Beam Scatterometer. *Remote Sens.* **2023**, *15*, 5063. [[CrossRef](#)]
13. Li, Z.; Verhoef, A.; Stoffelen, A.; Shang, J.; Dou, F. First Results from the WindRAD Scatterometer on Board FY-3E: Data Analysis, Calibration and Wind Retrieval Evaluation. *Remote Sens.* **2023**, *15*, 2087. [[CrossRef](#)]
14. Yun, R.; Dong, X.; Liu, J.; Lin, W.; Zhu, D.; Ma, J.; Lang, S.; Wang, Z. CFOSAT Rotating Fan-Beam Scatterometer Backscatter Measurement Processing. *Earth Space Sci.* **2021**, *8*, e2021EA001969. [[CrossRef](#)]
15. Soisuvann, S.; Jelenak, Z.; Chang, P.S.; Zhu, Q.; Shoup, C.G. High-Resolution Coastal Winds From the NOAA Near Real-Time ASCAT Processor. *IEEE Trans. Geosci. Remote Sens.* **2023**, *61*, 1–12. [[CrossRef](#)]
16. Ye, H.; Li, J.; Li, B.; Liu, J.; Tang, D.; Chen, W.; Yang, H.; Zhou, F.; Zhang, R.; Wang, S.; et al. Evaluation of CFOSAT Scatterometer Wind Data in Global Oceans. *Remote Sens.* **2021**, *13*, 1926. [[CrossRef](#)]
17. Singh, S.; Tiwari, R.K.; Sood, V.; Kaur, R.; Prashar, S. The Legacy of Scatterometers: Review of applications and perspective. *IEEE Geosci. Remote Sens. Mag.* **2022**, *10*, 39–65. [[CrossRef](#)]
18. Singh, S.; Tiwari, R.K.; Sood, V. Role of Ku-band (13.5 GHz) based Scatterometer Satellite (SCATSAT-1) in Cryospheric applications. In Proceedings of the 2023 IEEE International Geoscience and Remote Sensing Symposium, Pasadena, CA, USA, 16–21 July 2023.
19. Lin, W.; Dong, X.; Portabella, M.; Lang, S.; He, Y.; Yun, R.; Wang, Z.; Xu, X.; Zhu, D.; Liu, J. A Perspective on the Performance of the CFOSAT Rotating Fan-Beam Scatterometer. *IEEE Trans. Geosci. Remote Sens.* **2018**, *57*, 627–639. [[CrossRef](#)]
20. A Guide to NSIDC’s Polar Stereographic Projection, National Snow and Ice Data Center. Available online: <https://nsidc.org/data/user-resources/help-center/guide-nsidcs-polar-stereographic-projection> (accessed on 7 October 2023).

21. Spreen, G.; Kaleschke, L.; Heygster, G. Sea ice remote sensing using AMSR-E 89-GHz channels. *J. Geophys. Res.-Oceans* **2008**, *113*, C02S03. [[CrossRef](#)]
22. Melsheimer, C. *ASI Version 5 Sea Ice Concentration User Guide (Version V0.9.2)*; Institute of Environmental Physics, University of Bremen: Bremen, Germany, 2019.
23. OSI SAF/EARS Winds Team. *ASCAT Wind Product User Manual (Version: 1.17)*; EUMESTSAT, Ocean and Sea Ice SAF: Damstadt, Germany, 2021.
24. Contour-to-Contour Distance. Available online: <https://www.mathworks.com/matlabcentral/fileexchange/75551-contour-to-contour-distance> (accessed on 7 August 2023).
25. Long, D.G. Polar Applications of Spaceborne Scatterometers. *IEEE J. Sel. Top. Appl. Earth Obs. Remote Sens.* **2017**, *10*, 2307–2320. [[CrossRef](#)] [[PubMed](#)]
26. Rivas, M.B.; Otosaka, I.; Stoffelen, A.; Verhoef, A. A scatterometer record of sea ice extents and backscatter: 1992–2016. *Cryosphere* **2018**, *12*, 2941–2953. [[CrossRef](#)]
27. Shokr, M.; Ye, Y. Why Does Arctic Sea Ice Respond More Evidently than Antarctic Sea Ice to Climate Change? *Ocean-Land-Atmos. Res.* **2023**, *2*, 6. [[CrossRef](#)]
28. Sun, Y.; Ye, Y.; Wang, S.; Liu, C.; Chen, Z.; Cheng, X. Evaluation of the AMSR2 Ice Extent at the Arctic Sea Ice Edge using a SAR-based Ice Extent Product. *IEEE Trans. Geosci. Remote Sens.* **2023**, *61*, 1–15. [[CrossRef](#)]

Disclaimer/Publisher’s Note: The statements, opinions and data contained in all publications are solely those of the individual author(s) and contributor(s) and not of MDPI and/or the editor(s). MDPI and/or the editor(s) disclaim responsibility for any injury to people or property resulting from any ideas, methods, instructions or products referred to in the content.